RSC Advances

This article can be cited before page numbers have been issued, to do this please use: S. M. Patange, S. S. Desai, S. S. Meena, S. M. Yusuf and S. E. Shirsath, *RSC Adv.*, 2015, DOI: 10.1039/C5RA21522F.

ROYAL SOCIETY OF CHEMISTRY

www.rsc.org/advances

View Article Online
DOI: 10.1039/C5RA21522F

Random site occupancy induced disordered Néel-type collinear spin alignment in heterovalent Zn^{2+}-Ti^{4+} ions substituted $CoFe_2O_4$

S.M. Patange[a], S.S. Desai,[a] S. S. Meena,[b] S. M. Yusuf[b], Sagar E. Shirsath,[c]*

[a] Materials Research Laboratory, Shrikrishna Mahavidyalaya, Gunjoti 413613, MS, India
[b] Solid State Physics Division, Bhabha Atomic Research Centre, Mumbai 400085, India
[c] Spin Device Technology Center, Faculty of Engineering, Shinshu University, Nagano 380-8553, Japan

Abstract:

$CoFe_2O_4$, cobalt ferrite (CFO) nano-particles with composition $CoZn_xTi_xFe_{2-2x}O_4$ ($0 \le x \le 0.4$) were synthesized by sol-gel autocombustion method. The effect of Zn^{2+}-Ti^{4+} substitution on the structural, magnetic and frequency depended permeability properties of the CFO nano-particles were investigated by X-ray diffraction, ^{57}Fe Mössbauer spectroscopy, vibrating sample magnetometry, transmission electron microscopy and permeability analysis. The Rietveld refined XRD patterns confirm the single spinel phase and the crystallite size is found in the range of 22–32nm. Cation distribution was estimated by refining the XRD pattern by Rietveld method, and it is shows Zn^{2+} ions at tetrahedral A-site, Co^{2+} and Ti^{4+} ions at octahedral B-site. The saturation magnetization (Ms) increased from 58 to 75 emu/g up to x = 0.2 and then decreases, while the coercivity decreases continuously with Zn^{2+}-Ti^{4+} substitution. Two distinct composition ranges with Zn^{2+}-Ti^{4+} substitution are identified for which Ms variation with x is explained by the Néel and Yafet-Kittel models. The room temperature Mössbauer spectra are analyzed in detail for probing the magnetic properties of Fe based Zn^{2+}-Ti^{4+} substituted CFO. The effect of Zn^{2+}-Ti^{4+} substitution on various Mössbauer parameters viz hyperfine field distribution, isomer shift, quadrupole splitting and the line width has also been studied. The variation of nuclear magnetic fields at the A and B sites are explained on the basis of A-B and B-B supertransferred hyperfine interactions. The CFO nanoparticle is considered to possess a fully inverse spinel structure with a Néel-type collinear spin alignment, whereas the Zn^{2+}-Ti^{4+} substitution in CFO is found to be structurally and magnetically disordered due to the nearly random distribution of cations and the canted spin arrangement. The study also demonstrates that one can tailor the magnetic properties of CFO particles by optimizing the Zn^{2+}-Ti^{4+} substitution. The increase in the permeability, saturation magnetization and lower loss factor makes the synthesized materials suitable for their applications in microwave devices and deflection yoke.

Keywords: Ferrite nanoparticles; Crystal structure; Spin canting, Mössbauer spectroscopy, Permeability

*Corresponding author: Phone +9194233472 Fax No. +91-2475-250091
Email. smpatange@rediffmail.com

View Article Online
DOI: 10.1039/C5RA21522F

1. Introduction

Spinel ferrite crystal structure has the space group *Fd3m* ($F_{1/d}^{4}\bar{3}_{2/m}$, No. 227 in the International Tables) which consists of 56 atoms; 32 are oxygen anions assuming a close packed cubic structure, and the remaining are metal cations residing on 8 of the 64 available tetrahedral (A) sites and 16 of the 32 available octahedral (B) sites. The size and valence state of the cation species determine the filling of these sites and strongly influence the material's magnetic and electrical properties.

Cobalt ferrite (CFO) crystallizes in an inverse spinel structure. The inverse spinel form of CFO is represented generally as $A^{3+(TET)}[B^{2+}, B^{3+}]^{(OCT)}O_4$ where the tetrahedral A-sites are occupied by Fe^{3+} cations and octahedral B-sites are occupied by Fe^{3+} ions and the divalent Co^{2+} ions respectively.[1] In CFO, the magnetic interactions between these metal ions, limited only to the nearest neighbors, are antiferromagnetic in nature and their magnitudes are given by exchange integrals. For example, the exchange integral J_{AB} describes the nature and strength of the interaction between any two nearest A and B ions. Similarly, J_{AA}, J_{BB} and J_{AB} are the exchange integrals showing the strength of any A–A, B–B and A-B nearest neighbor interactions respectively. Generally, when the A and B sub-lattices are occupied by the magnetic ions of the same type, the relative strengths are given by $|J_{AB}| \gg |J_{BB}| > |J_{AA}|$: Thus, the moments on A- and B-sites are aligned anti-parallel to each other and this impels the two A-A and B-B moments to be parallel despite the antiferromagnetic exchange interactions between them, so these moments are in frustrated state. One can in principle alter the relative strengths of all these exchange integrals by changing the type of the magnetic ions on A and B sites.[2] CFO is widely used as a material for high-density data recording and storage systems,[3] biomedical hyperthermia inductors etc. [4,5] The requirements for the values of coercivity (Hc) depend on the application of CFO.

View Article Online
DOI: 10.1039/C5RA21522F

Characteristic values of coercivity for permanent magnets are 480–640kA/m and more, for magnetic recording 200–280kA/m and for biomedical applications as low as possible.[6] CFOs are being used for magnetic recording applications due to good intrinsic properties. These intrinsic magnetic properties, i.e. saturation magnetization (Ms) and coercivity (Hc) can be modified by the cationic substitution of Fe^{3+} ions. However, the substitution causes intrinsic Hc to decrease effectively at the expense of decrease in Ms, restricting their use for recording applications. Thus increasing efforts are being made to decrease coercive force and simultaneously increasing Ms with substitution. The value of the Ms must be high independent of application. Therefore, the preparation of CFO with high Ms and controlled Hc is a problem of today. In recent years, this problem is solved by heterovalent substitution of Fe^{3+} according to the scheme $2Fe^{3+}$-Me^{2+}+Me^{4+}, where Me^{2+} and Me^{4+} are ferromagnetic and nonmagnetic ions respectively. Such substitution ensures electrical neutrality in the CFO structure. Tailored coercivity materials, which might be of use in recording media such as hard discs, floppy discs and videotapes, can be prepared by the substitution of Co^{2+}–Ti^{4+},[7] Zn^{2+}–Ti^{4+},[8] Co^{2+}–Sn^{4+},[9] Mn^{2+}-Si^{4+},[10] Co^{2+}–Mo^{4+},[11] etc. ions into the ferrite.

Doping with aliovalent ions (Ti^{4+}) is used to break the coupling of ferrimagnetically active oxygen polyhedral in spinel ferrite. Ti^{4+} is believed that, are dissolved in the spinel matrix of the material and through this they directly affect the magnetic properties of the crystal structure. Zinc ferrite, $ZnFe_2O_4$, is a normal spinel, and such the unit cell has no net magnetic moment ($ZnFe_2O_4/Zn^{2+}[Fe^{3+}Fe^{3+}]O_4/d^0[d^5d^5]$). CFO is an inverse spinel and, consequently, the two magnetic sublattices are antiferromagnetically aligned ($CoFe_2O_4/Fe^{3+}[Co^{2+}Fe^{3+}]O_4/d^5[d^5d^5]$). When the nonmagnetic Zn^{2+} (d^{10}) is substituted into the CFO crystal lattice, it has a stronger preference for the tetrahedral site than does the ferric ion and thus reduces the amount of Fe^{3+} on

View Article Online
DOI: 10.1039/C5RA21522F

the A site. Because of the antiferromagnetic coupling, the net result is an increase in magnetic moment on the B lattice and an increase in saturation magnetization ($(Zn_x^{2+}Fe_{1-x}^{3+}[Co^{2+}Fe^{3+}]O_4/d_x^{10}d_{1-x}^{5}[d^5d^5])$. Therefore, in particular, it has been shown that Zn^{2+}–Ti^{4+} cationic mixtures produce materials with suitable characteristics for high-density magnetic recording. Also, it has been reported that site preference of Zn^{2+} ions can provoke an increase in the saturation magnetization, Ms, and reduce the switching field distribution (SFD) of the particles, which is an important parameter in magnetic recording applications.[12] On the other hand, the replacement of iron ions by Ti^{4+} on A-site can also increase Ms.[13] Ti^{4+} ion substitution at iron site in ferrites is known to be effective in reducing magnetocrystalline anisotropy and enhancing the electrical resistivity, these properties are suitable for wide range of industrial applications.[14]

Mössbauer spectroscopy is an effective method for investigating the local environment of nuclei, and namely the nature of the cationic site distribution. The presence of non-magnetic ions in spinel ferrites is found to alter their magnetic and electric properties. Such isomorphous substitutions in iron oxides are particularly apparent in their Mössbauer spectra, since these will drastically reduce magnetic interactions, resulting in lower magnetic ordering temperature and decreased magnetic field supertransfer (i.e., lower hyperfine fields).

In an attempt to shed more light on the origin of the magnetic changes when the substitutions are made, and in order to improve the Ms and Hc of CFO for specific application; the family of compounds, $CoZn_xTi_xFe_{2-2x}O_4$, where x ranges from 0.0 to 0.4, has been prepared and investigated using x-ray diffraction, vibrating sample magnetometer, permeability and Mössbauer spectroscopy.

View Article Online
DOI: 10.1039/C5RA21522F

2. Material synthesis and characterization

A series of spinel ferrite with formula $CoZn_xTi_xFe_{2-2x}O_4$ ($0 \leq x \leq 0.4$) was prepared by sol-gel auto combination method. All AR grade metal nitrates of Co, Zn, Ti and Fe were used for the synthesization of desired material. Citric acid ($C_6H_8O_7$) as a fuel was added into aqueous solution of metal nitrate. The metal nitrate to citric acid ($C_6H_8O_7$) ratio was kept as 1:3 and then the pH of the mixed solution was kept at 7 by adding ammonia solution. The mixed solution was evaporated to dryness by heating at 80 °C on a hot plate with continuous stirring and finally formed a very viscous brown gel. This viscous brown gel was ignited by increasing the temperature up to 100 °C and the loose powder of the samples was obtained. Finally, the as burnt powder was annealed at 600 °C for 4 h to obtain Zn^{2+}-Ti^{4+} substituted CFO ferrite nanoparticles. Chemical reaction of formula $CoZn_xTi_xFe_{2-2x}O_4$ is shown in Fig. 1.

The phase formation identification of samples prepared was characterized by X-ray diffraction (XRD, Philips X'Pert instrument) with Cu Kα radiation (wave length λ = 1.54056 Å) at room temperature. Transmission electron microscope (TEM) measurements were recorded on Philips (Model CM 200). Magnetic measurements were performed at room temperature using a commercial PARC EG&G vibrating sample magnetometer VSM 4500. Magnetic hysteresis loops were measured at room temperature with maximum applied magnetic fields up to 1 T.

The initial permeability (μ_i) measurements on the toroid-shaped samples were conducted as a function of frequency. The initial permeability measurements of the toroid samples were taken using a HP-4284A LCR precision meter. Mössbauer spectra of all the samples were recorded at room temperature using a Mössbauer spectrometer (Nucleonix Systems Pvt. Ltd., Hyderabad, India) operated at a constant acceleration mode (triangular wave) in transmission geometry at room temperature. The source employed was Co^{57} in Rh matrix of strength 50 mCi.

View Article Online
DOI: 10.1039/C5RA21522F

The calibration of the velocity scale is done by using an enriched α-^{57}Fe metal foil. The line width (inner) of calibration spectrum is 0.23 mm/s.

3. Results and discussion

3.1 Structural properties

Figure 2 demonstrates the Rietveld refined x-ray diffraction pattern of all the samples of $CoZn_xTi_xFe_{2-2x}O_4$ ferrite system. The pattern shows the formation of single phase cubic spinel structure with a space group Fd3m and without any signature of secondary phase. The data were processed to realize the conditions of the software program FullProf for the structure refinement. Crystal structure of the Zn^{2+}-Ti^{4+} substituted CFO were generated from the Rietveld refinement and same is presented in Fig. 3. All the results obtained from the refinement of the structure are correlated with Zn^{2+}-Ti^{4+} substitution. The values of discrepancy factor (R_{wp}) and expected (R_{exp}) values with goodness of fit (χ^2) index are given in Table 1. The XRD pattern shows the presence of (220), (311), (222), (400), (422) and (511). The analysis of XRD pattern reveals the formation of single phase cubic spinel ferrite and no extra peak other than cubic spinel phase is detected. The XRD pattern also shows slight shift in peak position toward lower 2θ angle due to the substitution of Zn^{2+} and Ti^{4+} ions. The lattice parameter was also calculated from the following relation:[15]

$$a_{xrd} = \frac{\lambda}{2}\left[\frac{\left(h^2+k^2+l^2\right)^2}{\sin\theta}\right] \quad (1)$$

Table 1 shows the variation of lattice parameter with Zn^{2+}-Ti^{4+} substitution calculated by using eq. 1 (a_{xrd}) and Rietveld method (a_{Riet}). Lattice constant of each sample were also calculated using the extrapolation function F(θ) i.e. the Nelson-Riley function for each reflection of the studied sample was calculated:[16]

View Article Online
DOI: 10.1039/C5RA21522F

$$F(\theta) = \frac{1}{2}\left[\left(\frac{Cos^2\theta}{Sin\theta}\right) + \left(\frac{Cos^2\theta}{\theta}\right)\right] \quad (2)$$

The values of the lattice constant 'a' are drawn in the Fig. 4 as a function of F(θ) for all x values. The relation in Fig. 4 represents straight line for each value of x. The true values of the lattice parameter 'a_0' can easily be obtained by extrapolating the line to the value F(θ) = 0 or θ = 90°. It is observed that lattice constant of CFO increased with increase in Zn^{2+}-Ti^{4+} substitution, this is due to the difference in combined ionic radii of Zn^{2+} (0.82Å) and Ti^{4+} (0.60 Å) that replaces Fe^{3+} (0.67Å) ions.

Average crystallite diameter 'D_{XRD}' of powder estimated from the most intense (311) peak of XRD and using the Scherrer method:

$$t_{XRD} = \frac{C\lambda}{B_{1/2}\cos\theta} \quad (3)$$

where $B_{1/2}$ is the full width of half maximum in (2θ), θ is the corresponding Bragg angle and C = 0.9. The values of crystallite diameter are presented in the Table 1. It is observed that particle size increased from 22-32 nm with increase in Zn^{2+}-Ti^{4+} substitution.

In order to study the morphology and phase structure of the synthesized samples, the samples were examined using transmission electron microscopy (TEM). Particle size determined from the TEM is in the range of 24-35 nm (Table 1). Fig. 5 shows TEM images of the typical samples (x = 0.0 and 0.4), that confirmed the particles are aggregated. Most of the nanoparticles appeared spherical in shape with small thickness. TEM image shows that the synthesized ferrite nanoparticles are agglomerated to some extent due to the interaction between magnetic nanoparticles.

View Article Online
DOI: 10.1039/C5RA21522F

Cation distribution: The cation distribution estimation was made from intensity ratio and using FullProf program. The data were processed to analyze using the computer Program FullProf.2 k (Version 4.30 -Apr2008-ILL JRC) in the Rietveld method for structure refinement. Program refinement of the first samples was started with the space group Fd3m, origin at -3 m, O in 32e-, A-site in 8f and B-site in 16c. In the first step the global parameters, such as 2θ-zero and background, were refined. In the next step, the structural parameters such as lattice parameter, atomic coordinates, and site occupancy, were refined. The fitting quality of the experimental data were checked by using the following parameters: the goodness of fit, χ^2; that must tend to one and two reliability factors, R_{exp} and R_{wp} (weighted differences between measured and calculated values) that must be close to or less than 10%.

Cation distribution of all the samples are obtained from the Rietveld refinement of X-ray diffraction patterns and presented in Table 2. The occupancies of some of the cations were fixed on the basis of their site preferences. It is known that Zn^{2+} ions have marked preference for tetrahedral A-site and similarly Co^{2+} ions have been reported to have strong preference for octahedral B-site due to their d^2sp^3 hybridization. But Co^{2+} ions were found not to occupy the A-sites and small percentage of Co^{2+} on A-site was deteriorating the agreement factors. Therefore, these cations were made to occupy their most preferential sites throughout the refinement. The Ti^{4+} ions are generally known to have octahedral (B) site preference.[17] Initially they were placed on the B-sites in the refinement model. However, the calculated profile could not be matched with the experimental one unless Ti^{4+} ions were allowed to occupy the A-sites also with small percentage.

The mean ionic radii of tetrahedral A-site (r_A), octahedral B-site (r_B), theoretical lattice parameter (a_{th}) and oxygen parameter (u) were calculated using the equations discussed

View Article Online
DOI: 10.1039/C5RA21522F

elsewhere.[18] The values of these parameters are listed in Table 3. It is observed that r_A increased whereas r_B decreased with Zn^{2+}-Ti^{4+} substitution. This behavior is directly related to site occupancy of cation at A and B site. It is observed that the variation of a_{th} is similar to a_{Riet} and a_{XRD}. The oxygen positional parameter 'u' is given by the distance between an oxygen ion and a face of a cube. In an ideal FCC structure u = 3/8 = 0.375 Å, where the packing of ions within the lattice is taken as perfect. The increased value in 'u' parameter may be associated with the shift of the origin at the tetrahedral sites with the decreasing number of Fe ion at the octahedral sites. That is, the distortion of the lattice, and the deviation from FCC ideal case. Further, the increasing value of u reveals the need for the structure to allow progressive expansion of the tetrahedral A-site so as to accommodate larger Zn^{2+} ions.

3.2 Permeability

Initial permeability (μ_i) investigation on the samples was carried out as a function of composition and frequency. Initial permeability showed dispersion at low frequency and decreases with frequency as shown in Fig. 6. Initial permeability would be due to the contribution from spin rotation and from the domain-wall motion. But the contribution from spin rotation is found to be smaller than domain-wall motion. It is mainly due to reversible motion of domain walls in the presence of weak magnetic field, and the contribution of spin rotation is negligible small.[19,20] The initial permeability contributed by domain-wall motion is expressed as;

$$\mu_i^w = 1 + \left(\frac{3}{16}\right)\frac{Ms^2 Dm}{\gamma_w} \qquad (4)$$

where *M*s is the saturation magnetization, *Dm* the average grain size and γw is the domain-wall energy. At low frequency, changes of the magnetization direction occur by the motion of domain walls, so that a domain oriented in the direction of the applied field grows at the expense of its

View Article Online
DOI: 10.1039/C5RA21522F

neighbours which are oriented in different direction. At higher frequency the domain wall is unable to move sufficiently rapidly to follow the alternating field. The overall magnetization vector does not follow the applied field hence accounting for the low value of permeability. The initial permeability in ferrites is known to be interplay of various factors like grain size (Dm), density, porosity, saturation magnetization (Ms), anisotropy (K_1), etc.:

$$\mu_i = \frac{\mu_0 Ms^2 Dm}{[K_1 + (3/2)\lambda s\sigma]\beta^{1/3}\delta} \quad (5)$$

where μ_i is the initial permeability, σ is stress, β is the volume concentration of impurity and δ is the thickness of domain wall. The permeability mechanism may be explained in terms of domain wall displacement and rotation of spins in each domain. It is observed that as the concentration of Zn^{2+}-Ti^{4+} is increased the grain size increases. According to Globus [19] a linear relationship exists between the grain diameter and permeability. The diameter of a Bloch wall is related to the grain size as the wall is taken to be fixed to the grain boundary along its circumference. As the size of the grains becomes larger, the domains and their wall motion would increase; causing the permeability to increase. The substitution of Zn^{2+}-Ti^{4+} is in CFO ferrite also increase particle size as discussed earlier which eventually enhance the densification and reduces the internal stress leading to decreasing magneto-crystalline anisotropy. This leads to a decrease in the hindrance given to the movement of domain walls resulting in increased value of μ_i.[21] The variation of magnetic loss factor (tanδ/ μ_i) with frequency is shown Fig. 7. The rapid increase in the loss factor at frequencies above 5 MHz may be attributed to the phenomenon of domain wall relaxation, which involves the hindrance of domain wall motions of small grains, by those of larger grains where the population of larger grains is smaller. The major contribution to the magnetic losses in ferrites is due to hysteresis losses, which in turn is based on damping phenomena associated with irreversible wall displacement and spin rotations. However, the

View Article Online
DOI: 10.1039/C5RA21522F

hysteresis loss becomes less important in the high-frequency range because the wall displacement is mainly damped and the hysteresis loss will be due to spin rotation.[22] It is observed that the values of loss factor decreased for x ≤0.2 with the increase in Zn^{2+}-Ti^{4+} substitution. The values of loss factor are also known to depend on various factors such as stoichiometry, Fe^{2+} content, and structural homogeneity, which in turn depend on the composition, and sintering temperature of the samples.[23] Because of low-melting point of Ti^{4+}, insulating phases may form at the grain boundaries, which could increase the electrical resistivity of the material. This has as a consequence of the reduction of the ohmic currents developed through the body of the material during operation under alternating currents and finally a reduction of the total power losses.[24] It is inferred from the present study that Zn^{2+}-Ti^{4+} ions have remarkably enhanced initial permeability of CFO and consequently the lower magnetic loss factor was observed. The magnetic loss factor values are found to be small even at higher frequencies for these samples, which is one of the criteria for the materials to be used in microwave devices and for deflection yoke.

3.3 Magnetization

Figure 8 shows hysteresis loops of Zn^{2+}-Ti^{4+} substituted CFO samples. It is observed from Figs. 8 and 9 that saturation magnetization (Ms) increased up to x = 0.2 and thereafter it decreases with increase in Zn^{2+}-Ti^{4+} substitution. The magnetic properties of Zn^{2+}-Ti^{4+} substituted CFO is depended on the site distribution of Zn^{2+}-Ti^{4+} ions and the strength of the exchange interaction among magnetic ions. The behavior in magnetization is related to following factors;

i) At x = 0.0, i.e. $CoFe_2O_4$, material posses inverse spinel structure with a Néel-type collinear spin alignment, where most of the Co^{2+} ions occupy octahedral B-site. When Zn^{2+}-Ti^{4+} ions are introduced at the cost of Fe^{3+} ions, most of the Zn^{2+} ions and some of

View Article Online
DOI: 10.1039/C5RA21522F

Ti^{4+} ions occupy A-sites in view of the site preferences for different ions as can be seen from cation distribution (Table 2). This increases the Fe^{3+} ion percentage at B-sites as compared to A-site. As a result, the magnetic moment of B sublattices increases at lower Zn^{2+}-Ti^{4+} substitution. According to Néel's two sublattice model of ferrimagnetism, the magnetic moments of ions on the A and B sublattices are aligned antiparallel to each other and in a collinear structure (Fig. 10a). However, as Zn^{2+}-Ti^{4+} substitution increases, A–B super exchange interactions become weak and B–B interactions start to dominate. Instead of collinear antiparallel alignment, a canted structure appears where the spins in B-sites are no longer parallel. The canted (non-collinear) spins naturally lead to a decrease in the value of the B-sublattice magnetization and thus the net magnetization falls off for x>0.2. The mechanism is presented schematically in Fig. 10.

ii) The magnetic moment of Zn^{2+} and Ti^{4+} is zero and for Fe^{3+} is 5 μ_B, the exchange interaction between Zn^{2+}- Ti^{4+} and Fe^{3+} ions being small, there will be canting of spins of Fe^{3+} and Zn^{2+} ions at the A site. The increase in the Zn^{2+}-Ti^{4+} content in the sample therefore decreases the magnetic moment of the A sublattice.

iii) It is expected that in the samples sintered at 600°C, some of the elements may evaporate. The melting point and the vapor pressure of Zn^{2+} and Ti^{4+} being the lowest, much lower than those for other elements, the probability of Zn^{2+} evaporation is maximum. There is a possibility of Fe_2O_3 formation as a result of zinc loss and this can alter the magnetic properties significantly. Any Zn^{2+} loss results in unsaturated oxygen bonds which tend to saturate by bonding with the surrounding B site Fe^{3+} ions reducing them to Fe^{2+}. This reduces the Fe^{3+} ion concentration at the B site. The B–B interaction thus becomes relatively weaker, resulting in an increase in magnetization of the B sublattice for lower

View Article Online
DOI: 10.1039/C5RA21522F

Zn^{2+}-Ti^{4+} substitutions. However, for higher Zn^{2+}-Ti^{4+} substitutions, there being more percentage of Fe^{3+} ions at the B site as compared to A-site, as indicated in point 'i' above, the increased B–B interaction reduces the magnetization of the B sublattice.

Here, processes 1 and 3 result in initial increase followed by a decrease in magnetization with increase in Zn^{2+}-Ti^{4+} substitution, process 2 increases the magnetization with increasing Zn^{2+}-Ti^{4+} substitution. The observed variation of magnetization in the present work is a sum total of these effects. The net magnetic moment (n_BCal.) is given by the sum of the magnetic moments of A and B sublattices, i.e., $M_S = M_B - M_A$. For Zn^{2+}-Ti^{4+} substituted CFO, most of the Zn^{2+}-Ti^{4+} ions replaces Fe^{3+} ions at A site, leading to a increase in the B-site sublattice magnetization. We use the known magnetic moments for Co^{2+} ($3\mu_B$), Zn^{2+} ($0\mu_B$), Ti^{2+} ($0\ \mu_B$) and Fe^{3+} ($5\mu_B$). In this study, the cationic distribution, Zn^{2+} and Ti^{4+} ions are non-magnetic and do not contribute to the sublattice magnetization.

The observed magnetic moment (n_BObs.) per formula unit in Bohr magneton (μ_B) was calculated by using the relation:

$$n_B Obs\ . = \frac{M_W \times M_S}{5585} \qquad (6)$$

where M_W is the molecular weight of the sample, n_B is the magnetic moment of the samples expressed in Bohr magneton, Ms is the saturation magnetization. The variation in observed and calculated magnetic moment is shown in Fig. 11. The increasing nature of magneton number can be explained on the basis of Néel two sub-lattice model.[25] The decreasing trend for $x > 0.2$ is due to the nonzero Yafet-Kittel (Y-K) angles in the samples that cannot be explained on the basis of the Néel's two sub-lattice model. This suggests that there are triangular type spin arrangements on B sites (Fig. 10b) which weaken A–B interaction. Further increase in Zn^{2+}-Ti^{4+} substitution

View Article Online
DOI: 10.1039/C5RA21522F

decreases the strength of the exchange interactions, and leads to the lower value of the saturation magnetization and observed magnetic moment.

The existence of canted spins and reduced magnetic moment with Zn^{2+}-Ti^{4+} substitution can be observed by determining the Yafet–Kittel angle:[26]

$$n_B = (6 + x) \cos \alpha_{Y-K} - 5\,(1 - x) \quad (7)$$

where x represents Zn^{2+}-Ti^{4+} substitution. It increases exponentially with the increase in Zn^{2+}-Ti^{4+} substitution for $x > 0.2$ as observed in the inset of Fig. 11. Furthermore, one reasonably believes that the increase in the Y-K angle of magnetic ions means that a decrease in the overlap of the wave functions between two nearest-neighbouring magnetic ions as well as that between magnetic ions and oxygen anions, leads to a reduction in superexchange interactions occurring between the magnetic ions and mediated by the intervening oxygen anions.[27] This shows that in the present system of ferrites, randomness increases as Zn^{2+}-Ti^{4+} is substituted in CFO and shows a significant departure from Néel collinear model.

Coercivity: It is observed from Figs. 8 and 9 that coercivity decreased from 852 to 112 Oe. This can be related to increase in particle size with Zn^{2+}-Ti^{4+} substitution. As the particle size decreases below a critical size or magnetic exchange length, L_{ex}, Hc follows a D^6 power law:[28]

$$Hc = \frac{PcK_1^4 D^6}{\mu_0 MsA^3} \quad (8)$$

where A is the exchange stiffness constant, and PC is a constant of the order of unity. Lex can be expressed as $L_{ex} = \sqrt{A/K_1}$. The critical size of Co–ferrites for the single domain behavior, depending on composition, is between 30 and 70 nm.[29] That is, for $D \gg D_{Crit}$, one would expect Hc to decrease by increasing the crystallite size as th+e system enters the multidomain region. The decrease in Hc is also related to magneto-crystalline anisotropy, the large coercivity in bulk

View Article Online
DOI: 10.1039/C5RA21522F

stoichiometric CFO has traditionally been explained by the single-ion anisotropy model, arising from the contribution of the orbital magnetism of Co^{2+} ions at the [B] sites ($CoFe_2O_4$, high-spin Co^{2+} ions).[30] That is, when the Co^{2+} ions migrate from the octahedral sites to the tetrahedral ones because of the variations in the inversion, the coercivity decreases due to the less anisotropic environment of the tetrahedral sites. CFO is only weakly anisotropic at room temperature because of the presence of low-spin Co^{2+} ions. Another reason is the angular momentum of the zinc ion. Zn^{2+} has a zero angular momentum (l=0) and does not contribute to magneto-crystalline anisotropy; consequently, the magnetic anisotropy and magnetic coercivity will decrease.

3.4 Mössbauer spectroscopy

Mössbauer spectroscopy is a powerful technique to investigate the magnetic properties of magnetic nanoparticles, which depends on various factors viz., particle size, measurement time window and magnetic anisotropy. If the magnetization direction of a magnetic nanoparticle fluctuates in a time greater than 10 ns, Mössbauer platform can detect the presence of magnetic hyperfine field and correspondingly a six line pattern has been generated. On the other hand, when the time of fluctuation τ is less than 10 ns, the time average of the hyperfine field created by the magnetic moment at the nuclear site becomes zero over the measurement time of the Mössbauer effect and consequently the Mössbauer spectrum will be double corresponding to the quadrupole splitting of the ^{57}Fe nucleus.[31, 32]

The Mössbauer spectrum of the sample x = 0.0 exhibit normal Zeeman split two sixtet along with a very week signature of doublet pattern in the central region. Among the two sixtet one due to the Fe^{3+} ions at the tetrahedral A-sites, the other due to the Fe^{3+} ions at the octahedral B-sites. The observed Mössbauer pattern also indicates that the nanoparticles are in the ordered ferrimagnetic state. The presence of the low intense doublet for x= 0.0 could be interpreted by

View Article Online
DOI: 10.1039/C5RA21522F

the presence of a small fraction of super-paramagnetic phase, perhaps due to a bilobar size distribution of ferrite particles. The sample with x = 0.4; Mössbauer spectrum consists of doublet and week sextet patterns and shows a relaxation behavior. The primary features of the relaxation spectrum for a magnetically ordered system are a significant broadening of Zeeman lines and a growth of the inner lines arise expense of the outer lines. For x = 0.4, the A site magnetic ion concentration is near to the site percolation threshold for the A site; this effect may be because of the presence of finite clusters together with an infinite magnetic network. The week sextet pattern in this sample indicates the presence of a small fraction of magnetic ordered particles and the intense doublet pattern indicates that the majority of particles are ultrafine particles with either superparamegnetic or paramagnetic behavior. A superimposed quadrupole doublet for x = 0.4, indicating a canted ferromagnetic structure characterized by a significant reduction of magnetic hyperfine field or by the collapse of sextets. It is worth noticing that, the Mössbauer spectra reveal a relaxation as Zn^{2+}-Ti^{4+} substitution increases as also evidenced by the increase in linewidth (Γ) of octahedral B-site with increasing Zn^{2+}-Ti^{4+} substitution. In the presence of a paramagnetic hyperfine interaction, the following two characteristic times have to be considered: the relaxation time of the electroin spin (spin-spin and spin-lattice) τ_s and the nuclear Larmor precession time τ_L. If $\tau_s \gg \tau_L$, a 'static' nonvanishing hyperfine interaction is present at the nucleus and a hyperfine spectrum with sharp lines is expected. If $\tau_s \ll \tau_L$, the hyperfine interaction produces an average value as a result of the rapidly fluctuating electron spins and the splitting collapse. Under the condition $\tau_s \approx \tau_L$, complicated spectra with broad lines are found. This allows an estimation of electron relaxation time to be made.

Quadrupole splitting (*QS*): The values of QS as obtained from Mössbauer spectra is depicted in Table 4. The presence of chemical disorder in the spinel structure produces an electric field

View Article Online
DOI: 10.1039/C5RA21522F

gradient (EFG) of varying magnitude, direction, sign and symmetry and a resulting distribution in the QS. The EFG at ^{57}Fe nucleus arises from the asymmetrical charge distribution surrounding the ion. However, since an Fe^{3+} ion has a half-filled 3d shell ($3d^5$), the EFG in this case can arise only from an asymmetric charge distribution surrounding the iron ion. In a cubic system having Fe^{3+} at both A- and B-sites, the A-site shows a QS due to the asymmetric charge distribution from the 12 B-neighbors. Fe^{3+} ion at B-site has trigonal symmetry and therefore B-sublattice exhibits an EFG with its principal component Vzz along the [111] direction. This EFG may arise from departure of the six nearest anion neighbors from their ideal octahedral symmetry and, the non-spherical distribution of charges on the next nearest cation and anion neighbors of the B-site. In the present case nearly zero values of QS within the experimental error is an indication that the cubic symmetry is retained between the Fe^{3+} ions and its surrounding comprising Zn^{2+}-Ti^{4+} substituted CFO nanoparticles.

Hyperfine magnetic field (H_{hf}): The Mössbauer study is also crucial to draw any quantitative conclusions regarding the distribution of hyperfine fields (H_{hf}) at A- and B-site, which is imperative for in depth analysis of magnetic interactions of these materials. In general the hyperfine field is given as:[33]

$$H_{hf} = H_{core} + H_{STHF} + H_{THF} + H_D \quad (9)$$

where H_{core} is the field due to the polarization of core s-electrons, H_{THF} is the transferred hyperfine fields, H_D is the dipolar field contribution and H_{STHF} is the supertransferred field associated. The H_{STHF} at site-A is due to the spin transfer from the d-orbitals of the nearest neighbor cation sites (i.e. belonging to sublattice-B) to the s-orbitals of the ion under consideration at site-A through the ligand anions. Thus STHF at site-A will depend on the magnetic moment of the ions at site-B. In the present case the variation in hyperfine field is due

View Article Online
DOI: 10.1039/C5RA21522F

to H_D and H_{STHF} only because H_{core} and H_{THF} do not vary much on changing Zn^{2+}-Ti^{4+} substitution. The effects due to H_D are also negligible and they mainly cause the line broadening. In light of this, the eq. (9) gets modified as; $H_{hf} = H_{STHF}$.[34, 35] From Table 4 small variation in H_{hf} distribution at A- and B-site is observed. This reflects that H_{hf} at A-site is not much sensitive to any change in the number and kind of cations at B-site. Thus the changes in H_{hf} are mainly due to the non-dynamical effects arising from the supertransferred hyperfine interactions (STHF),[34, 36] when the cation's neighbors around Fe ions are changed. STHF components are strongly influenced by the super-exchange coupling and magnetic moments of cations. In CFO with spinel structure, each tetrahedral Fe^{3+} ion has strong super-exchange coupling with 12 neighboring metal ions present on the octahedral sites. The replacement of any of Fe^{3+} ions at A-site with Zn^{2+} and Ti^{4+} ions bring small change in super-exchange interaction to cause a significant change in magnetic moments and hence STHF, is responsible for variation in present H_{hf} at A-site. For octahedral B-site; Fe^{3+} ion is coupled via super-exchange coupling to only 6 neighboring metal ions present at A-site. The replacement of octahedral B-site Fe^{3+} ions by Ti^{4+} is generally expected to bring significant changes in STHF and hence H_{hf}. Though, this explanation is not good enough to understand the observed change in the H_{hf} at A- and B-site. Therefore, significant canting as discussed above in magnetization results must be taken into consideration for the analysis of H_{hf} spectra. Since STHF components are assumed to depend upon a collinear spin arrangement and spin canting in the samples is not allowing STHF components to contribute effectively to the resultant H_{hf}. It is observed from Table 4 that H_{hf} of octahedral B-site is slightly increased up to x = 0.2 and then decreased further with Zn^{2+}-Ti^{4+} substitution. Hence it may be concluded that the change in magnetization upon introducing the Zn^{2+}-Ti^{4+} impurity is not only due to the simple replacement of Fe^{3+} ions by non-magnetic Zn^{2+}-

View Article Online
DOI: 10.1039/C5RA21522F

Ti^{4+} ions but also due to a more complex process which leads to the development of canted spin structure. According to Néel's molecular field model,[37] A-B exchange interactions are stronger than that of A-A or B-B interactions. In the above mentioned cation distribution Zn^{2+} and Ti^{4+}, being diamagnetic, do not take part in the exchange interaction. The $Fe_B^{3+} - O^{2-} - Co_B^{3+}$ super exchange interaction is weaker than the $Fe_B^{3+} - O^{2-} - Fe_B^{3+}$ interaction. The net magnetic field is mainly due to average $Fe_B^{3+} - O^{2-} - Fe_B^{3+}$ magnetic bonds per Fe^{3+} ions. The observed behavior in the present case is assigned to the dominance of $Fe_B^{3+} - O^{2-} - Fe_B^{3+}$ interactions and large occupancy of Zn^{2+} ions at A-site. Further, it can be argued that the entry of Ti^{4+} in the lattice causes orientational relaxation of the spins thereby modifying the strength of the exchange interactions.[38] The decrease in H_{hf} for x>0.2 is due to the larger occupancy of Ti^{4+} ions at B-sites. Also the replacement of Fe^{3+} ($5\mu_B$) ions with non magnetic Zn^{2+}-Ti^{4+} ($0\ \mu_B$) ion reduces the strongest $Fe_A^{3+} - O^{2-} - Fe_B^{3+}$ interactions and hence H_{hf} is expected to decrease at higher Zn^{2+}-Ti^{4+} substitution level. These results are also well supported by Rietveld refined cation distribution and magnetization results.

Isomer shift (*IS*): Table 4 represents the variation of the isomer shift as a function of x, for Fe^{3+} ions at tetrahedral A- and octahedral B-sites. It is observed that IS at B-site is greater than IS at A-site, this could be interpreted as being due to the large band separation of Fe^{3+}-O^{2-} for the octahedral ions compared with that for the tetrahedral ions. As the orbitals of the Fe^{3+} and O^{2-} ions do not overlap, the co-valency effect becomes smaller, and hence the isomer shift is large at the octahedral site. IS at A and B-site appear no significant variation with Zn^{2+}-Ti^{4+} substitution, thus indicating that the s-electron charge distribution of the Fe^{3+} ions is not influenced by Zn^{2+}-Ti^{4+} substitution. The range of values of isomer shift indicates that iron exists in Fe^{3+} valence state with high spin configuration in the prepared samples.

View Article Online
DOI: 10.1039/C5RA21522F

Linewidth (*Γ*): The linewidth values corresponding to A- and B-sites have been found to increase for B-site from 0.345 to 1.036 mm/s and for A-site increased from 0.303 (x=0.0) to 0.369 (x=0.1) mm/s followed by decreasing trend to 0.230 mm/s (x=0.4) with increasing Zn^{2+}-Ti^{4+} substitution (Table 4). It has been observed that the linewidths at tetrahedral A-sites are smaller than those at octahedral B-sites for the whole range of Zn^{2+}-Ti^{4+} substitution. The broadening of linewidths could be attributed to slight changes in the varying environment surrounding Fe^{3+} ions in the same sub lattice; such changes in environment of Fe^{3+} ions would lead to a change in the magnetic field and consequently result in an appreciable broadening of the Zeeman lines. The increased broadening in the lines at B-site with an increase in Zn^{2+}-Ti^{4+} substitution may be attributed to large number of probable distribution of Zn^{2+}-Ti^{4+} ions surrounding Fe^{3+} nuclei at B-sites. On the other hand decreasing trend of linewidth for A-site ($x \leq 0.1$) is ascribed to the reducing number of Fe^{3+} ions from A-site with every substitution of Zn^{2+}-Ti^{4+} ions.

4. Conclusions

The XRD analysis showed that the prepared $CoZn_xTi_xFe_{2-2x}O_4$ ($0 \leq x \leq 0.4$) samples are the single phase cubic structure. All the samples fitted with Rietveld refinement using FullProf program revealed the existence of cubic structure (space group Fd3m). Lattice constant and particle size of CFO found to increase with Zn^{2+}-Ti^{4+} substitution. Cation distribution estimated from Rietveld refinement shows Zn^{2+} ions have occupy tetrahedral A-site only whereas $Ti^{4+}$and Co^{2+} ions shows strong preference towards octahedral B-site. Quantitative information on the distribution of local magnetic fields and on the canted spin arrangement of Zn^{2+}-Ti^{4+} substituted CFO nanoparticles provided by Mössbauer spectroscopy is complemented by investigations of

View Article Online
DOI: 10.1039/C5RA21522F

their magnetic behavior on the macroscopic scale. For pure CFO Mössbauer exhibits well defined Zeeman sextet corresponding to tetrahedral and octahedral sites, whereas relaxation behavior is observed for x = 0.4. Hyperfine field shows small variation with Zn^{2+}-Ti^{4+} substitution, which has been explained in terms of supertransfer hyperfine field interactions and observed significant canting in the samples. Hyperfine field at A-site and saturation magnetization showed increased value for x = 0.2 followed by decreasing trend with Zn^{2+}-Ti^{4+} substitution. Zn^{2+} ions because of its occupancy towards tetrahedral A-sites have greater impact on the magnetic properties as compared to that of Ti^{4+} ions. However the contribution from Ti^{4+} for the enhancement in the magnetic properties cannot be neglected. Therefore the variation in magnetic properties of cobalt ferrite is the combined effect of both Zn and Ti ions. Real part of permeability of CFO increased with complete range of Zn^{2+}-Ti^{4+} substitution.

References

1 B. G. Toksha, Sagar E. Shirsath, M. L. Mane, S. M. Patange, S. S. Jadhav and K. M. Jadhav, *J. Phys. Chem. C* 2011, **115**, 20905–20912.

2 K. H. Jani, K.B. Modi, H.H. Joshi, P.D. Babu and S.K. Paranjpe, *J. Magn. Magn. Mater.,* 2004, **280**, 334–345.

3 S.K. Gore, R.S. Mane, Mu. Naushad, S.S. Jadhav, M.K. Zate, Z. A. Alothman and Biz K. N. Hui, *Dalton Trans.*, 2015, **44**, 6384-6390.

4 V. Georgiadou, C. Kokotidou, B. Le Droumaguet, B. Carbonnier, T. Choli-Papadopoulou and C. Dendrinou-Samara, *Dalton Trans.,* 2014*,* **43**, 6377-6388.

5 S. Mohapatra, S. R. Rout, S. Maiti, T. K. Maiti and A. B. Panda, *J. Mater, Chem.,* 2011, **21**, 9185-9193.

View Article Online
DOI: 10.1039/C5RA21522F

6 E.D. Solovyova, E.V. Pashkova, V.P. Ivanitski, O.I. Vyunov and A.G. Belous, *J. Magn. Magn. Mater.,* 2013, **330**, 72–75.

7 Koichi Watanabe and Junko Kawabe, *J. Mater. Chem.*, 1997, **7,** 1797-1800.

8 P. Wartewig, M.K. Krause, P. Esquinazi, S. Rosler and R. Sonntag, *J. Magn. Magn. Mater.*, 1999, **192**, 83.

9 X. Batlle, M. Pernet, X. Obradors, in: Proceedings ICF-5, India, 1989. p. 423.

10 R.H. Kadam, Kirti Desai, Supriya R. Kadam and Sagar E. Shirsath, *Solid State Sci.,* 2013, **26**, 31-37

11 D.G. Agresti, T.D. Shelfer, Y.K. Hong and Y. J. Paig, *IEEE Trans. Magn.*, 1989, **25** 4069.

12 O. Kubo and E. Ogawa, *J. Magn. Magn. Mater.,* 1994, **134**, 376.

13 A. Gonzalez-Angeles, G. Mendoza-Suarez, A. Gruskova, M. Papanova and J. Slama, *Mater. Lett.,* 2005, **59**, 26–31.

14 M.A. Ahmed, K.E. Rady and M.S. Shams, *J. Alloy. Compd.*, 2015, **622**, 269–275

15 B. D. Cullity, "Elements of X-ray diffraction", Addison-Wesley Publ. Comp. Inc., Reading, Massachusetts, USA (1956), 99.

16 Sagar E. Shirsath, Santosh S. Jadhav, B. G. Toksha, S. M. Patange and K. M. Jadhav, *J. Appl. Phys.*, 2011, **110**, 013914.

17 G. Gavollie, J. Hubsch, *J. Magn. Magn. Mater.*, 1983, **36**, 304.

18 Sagar E. Shirsath, Mahesh L. Mane, Yukiko Yasukawa, Xiaoxi Liu and Akimitsu Morisako, *Phys. Chem. Chem. Phys*., 2014, **16**, 2347

19 A. Globus, P. Duplex and M. Guyot, *IEEE Trans. Magn. Mag-7* 1971, **3**, 617–622.

20 A. Globus and P. Duplex, *J. Appl. Phys.*, 1968, **39**, 727–729.

View Article Online
DOI: 10.1039/C5RA21522F

21 J. Smit and H.P.J. Wijn, Ferrites, Philips Technical Library, Einthoven, Netherland, 1959, p.275.

22 S. Chikazumi, Physics of Magnetism, Wiley, New York, 1964, p. 263.

23 A. Lakshman, P.S.V. Subba Rao and K.H. Rao, *J. Magn. Magn. Mater.*, 2004, **283**, 329–334

24 V.T. Zaspalis, E. Antoniadis, E. Papazoglou, V. Tsakaloudi, L. Nalbandian and C.A. Sikalidis, *J. Magn. Magn. Mater.*, 2002, **250**, 98–109.

25 L. Néel. Comptes-rendus *Acad. Sci. Paris,* 1950, **230**, 375.

26 Y. Yafet and C. Kittel, *Phys. Rev.,* 1952, **87**, 290–294.

27 W. F. Pong, Y. K. Chang, M. H. Su, P. K. Tseng, H. J. Lin, G. H. Ho, K. L. Tsang and C. T. Chen, *Phys. Rev. B*, 1997, **55**, 11409-11413.

28 Q. Zeng, I. Baker, V. McCreary and Z. Yan, *J. Magn. Magn. Mater.*, 2007, **318**, 28–38.

29 A.E. Berkowitz and W.J. Schuele, *J. Appl. Phys.*, 1959, **30**, S134–S134.

30 G. Salazar-Alvarez, R.T. Olsson, J. Sort, W.A.A. Macedo, J.D. Ardisson, M.D. Baro´, U.W. Gedde and J. Nogues, *Chem. Mater.*, 2007, **19**, 4957–4963.

31 S. Morup, Science & Technology of Nanostructured Magnetic Materials in G.C. Hadjipanayis, G.A. Prinz (Eds.), Plenum, NY, USA, 1991, P. 545

32 S. Sutradhar, S. Pati, S. Acharya, S. Das, D. Das and P.K. Chakrabarti, J. *Magn. Magn. Mater.*, 2012, **324**, 1317-1325

33 W. Marshal, *Phys. Rev.*, 1958, **110**, 1280-1285

34 L. K. Leung, B.J. Evans and A.H. Morrish, *Phys. Rev. B*, 1973, **8**, 29-43

35 D. Peddis, N. Yaacoub, M. Ferretti, A. Martinelli, G. Piccaluga, A. Musinu, C. Cannas, G. Navarra, J.M. Greneche and D. Fiorani, *J. Phys.: Condens. Matter*, 2011, **23**, 426004. 1-8.

View Article Online
DOI: 10.1039/C5RA21522F

36 G. A. Sawatzky, F.V.D. Woude and A. H. Morrish, *J. Appl. Phys.*, 1968, **39**, 1204-1206.

37 L. Néel, *Ann Phys.* 1948, **3**, 137

38 Prem Chand, R.C. Srivastava and Anuj Upadhyay, *J. Alloy. Compd.*, 2008, **460**, 108–114.

Table 1 Discrepancy factor (R_{wp}), expected values (R_{exp}), goodness fit factor (χ^2), lattice constant (a_{xrd} and a_{Riet}), crystallite size (t_{xrd}) and particle size (t_{TEM}) of $CoZn_xTi_xFe_{2-2x}O_4$

x	R_{exp}	R_{wp}	χ^2	'a_{xrd}'	'a_{Riet}'	t_{xrd}	t_{TEM}
0.0	4.5	3.5	1.65	8.3864	8.3668	22	24
0.1	3.6	3.6	1.00	8.3949	8.3989	24	28
0.2	8.2	8.1	1.02	8.4019	8.4019	28	27
0.3	9.5	8.4	1.28	8.4068	8.4093	28	31
0.4	6.5	5.2	1.56	8.4122	8.4132	32	35

Table 2: Values of atomic coordinates (x, y, z) and occupancy (g) determined from Rietveld refinement of XRD pattern of $CoZn_xTi_xFe_{2-2x}O_4$.

Atom	x=0.0		x=0.1		x=0.2		x=0.3		x=0.4	
	x=y=z	Occ.(g)	x=y=z	Occ.(g)	x=y=z	Occ.(g)	x=y=z	Occ.(g)	x=y=z	Occ.(g)
Co	0.1250	0.0998(2)	0.1250	0.1002(2)	0.1250	0.1100(3)	0.1250	0.1405(2)	0.1250	0.1604(3)
Zn	0.1250	0.0000	0.1250	0.0999(1)	0.1250	0.1998(2)	0.1250	0.3000(1)	0.1250	0.3999(1)
Ti	0.1250	0.0000	0.1250	0.0204(1)	0.1250	0.0399(1)	0.1250	0.0400(2)	0.1250	0.0500(1)
Fe	0.1250	0.8998(2)	0.1250	0.7800(1)	0.1250	0.6495(2)	0.1250	0.5192(1)	0.1250	0.3891(2)
Co	0.5000	0.8999(2)	0.5000	0.8999(1)	0.5000	0.8895(2)	0.5000	0.8590(3)	0.5000	0.8393(1)
Ti	0.5000	0.0000	0.5000	0.0796(1)	0.5000	0.1599(1)	0.5000	0.2599(1)	0.5000	0.3499(1)
Fe	0.5000	1.0999(1)	0.5000	1.0200(2)	0.5000	0.9503(2)	0.5000	0.8806(1)	0.5000	0.8106(1)

Table 3: Mean ionic radii at tetrahedral A-site (r_A), octahedral B-site (r_B), theoretical lattice constant (a_{th}) and oxygen positional parameter (u) of $CoZn_xTi_xFe_{2-2x}O_4$

x	A site (r_A)	B- site (r_B)	a_{th}	u
0.0	0.612	0.692	8.342	0.3837
0.1	0.636	0.690	8.371	0.3849

View Article Online
DOI: 10.1039/C5RA21522F

0.2	0.659	0.687	8.399	0.3861
0.3	0.685	0.682	8.428	0.3874
0.4	0.710	0.679	8.457	0.3886

Table 4

The relative intensity (RI) in percentage, linewidth (Γ), isomer shift (*IS*), quadrupole splitting (*QS*), Hyperfine magnetic field (H_{hf}) and Fitting quality (χ^2) of tetrahedral and octahedral sites of Fe^{3+} ions for $CoZn_xTi_xFe_{2-2x}O_4$ (x = 0.0, 0.1, 0.2, 0.3 and 0.4) ferrite derived from Mössbauer spectra recorded at room temperature. Isomer shift values are relative to Fe metal foil (δ = 0.0 mm/s). Sextet A: Tetrahedral site, Sextet B: Octahedral site

(*x*)	Iron Sites	RI (%)	Γ (mm/s)	IS (mm/s)	QS (mm/s)	H_{hf} (Tesla)	χ^2
0.0	Doublet	0.65	0.486344 (±0.30613)	0.248804 (±0.06177)	0.220520 (±0.20587)		1.47
	Sextet A	66.79	0.303150 (±0.01942)	0.160103 (±0.00292)	-0.015068 (± 0.00482)	49.251087 (±0.01752)	
	Sextet B	32.55	0.345018 (±0.03291)	0.438774 (±0.00719)	0.148615 (±0.01234)	50.252955 (±0.05037)	
0.1	Sextet A	58.55	0.369817 (±0.04594)	0.263995 (±0.00410)	-0.011570 (±0.00728)	47.960246 (±0.04925)	1.19
	Sextet B	41.45	0.694491 (±0.08087)	0.341672 (±0.01697)	-0.065510 (±0.03088)	51.688579 (±0.43506)	
0.2	Sextet A	43.95	0.286968 (±0.03970)	0.265465 (±0.00397)	0.014301 (±0.00769)	46.542426 (±0.05137)	1.21
	Sextet B	56.05	0.773426 (±0.04485)	0.326947 (±0.01238)	-0.038131 (±0.02337)	54.413692 (±0.28624)	
0.3	Sextet A	38.60	0.230000 (±0.00000)	0.310329 (±0.00836)	0.001764 (±0.01613)	43.774676 (±0.11353)	1.26
	Sextet B	61.40	1.036929 (±0.05963)	0.379229 (±0.02182)	-0.001109 (±0.04148)	37.016382 (±0.37511)	
0.4	Doublet	9.02	0.428724 (±0.01903)	0.348579 (±0.00564)	0.483531 (±0.00949)		0.94
	Sextet A	16.22	0.230000 (±0.0000)	0.265474 (±0.02325)	0.059268 (±0.04536)	43.324537 (±0.30949)	
	Sextet B	74.74	0.801281 (±0.07384)	0.366924 (±0.02303)	0.042567 (±0.04260)	37.280437 (±0.36079)	

View Article Online
DOI: 10.1039/C5RA21522F

Fig. 1: Chemical reaction of $CoZn_xTi_xFe_{2-2x}O_4$ synthesized by sol-gel autocombustion method.

View Article Online
DOI: 10.1039/C5RA21522F

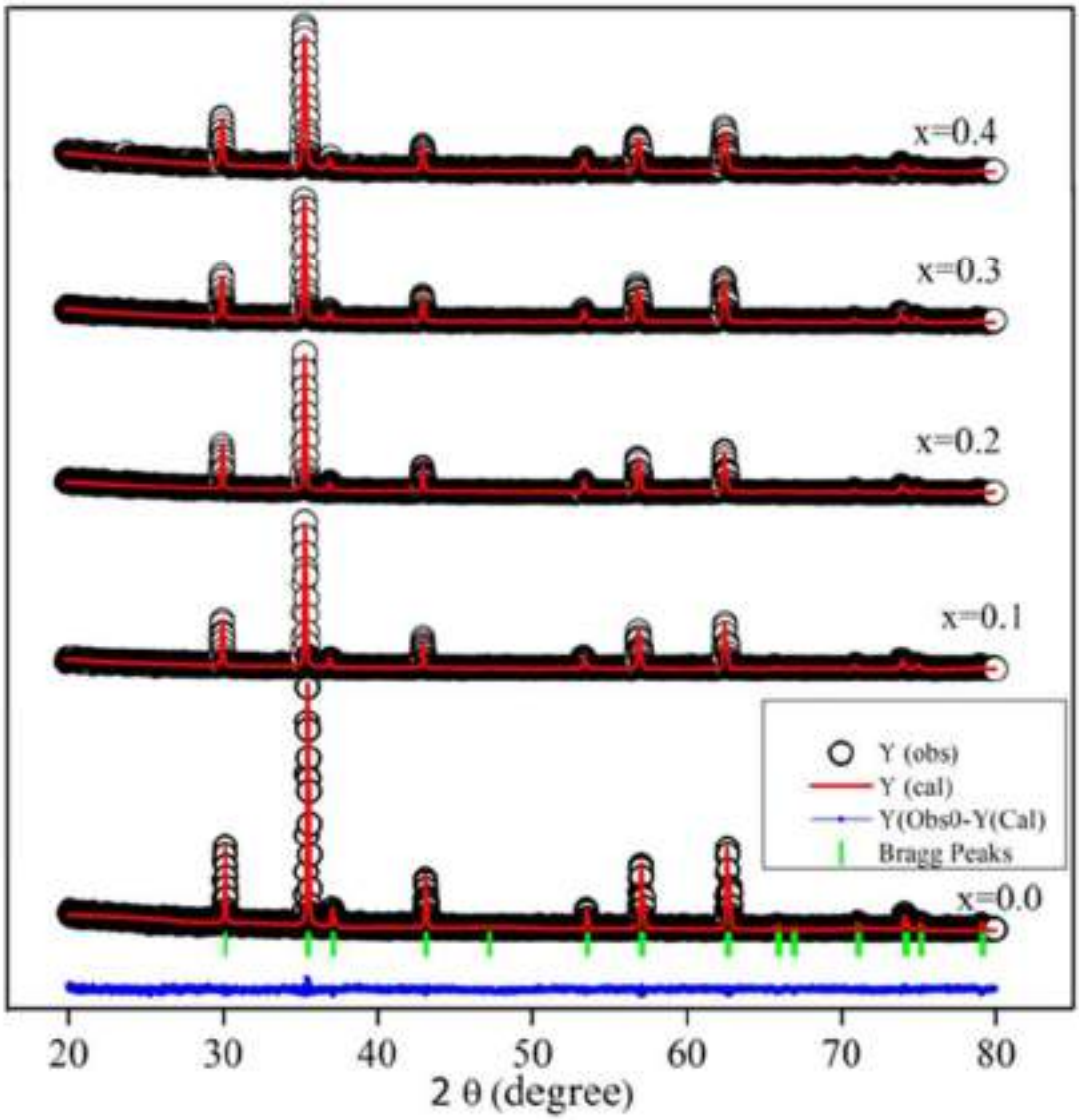

View Article Online
DOI: 10.1039/C5RA21522F

Fig. 2. Rietveld refined X-ray diffraction patterns of $CoZn_xTi_xFe_{2-2x}O_4$

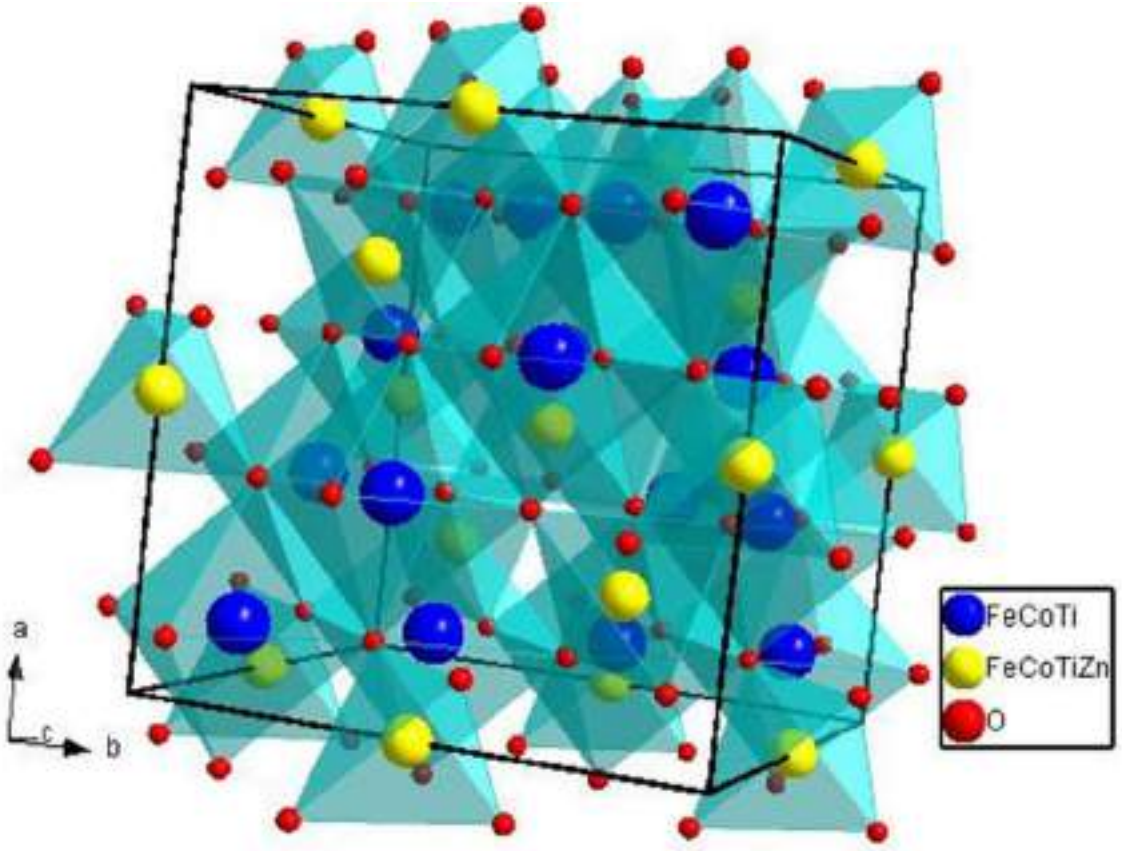

Fig. 3. Cubic spinel crystal structure of $CoZn_xTi_xFe_{2-2x}O_4$ (x = 0.2)

View Article Online
DOI: 10.1039/C5RA21522F

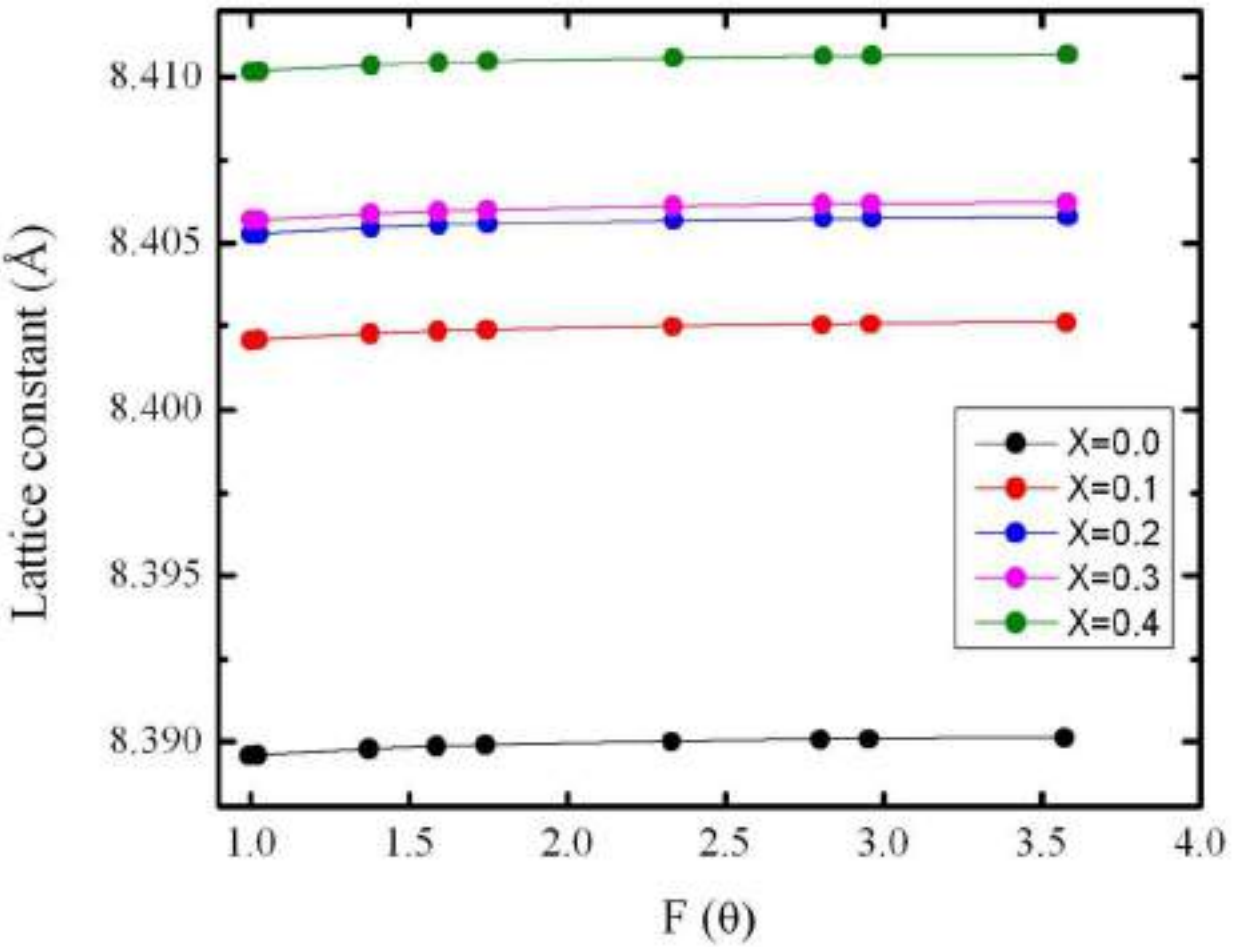

View Article Online
DOI: 10.1039/C5RA21522F

Fig. 4. Variation of lattice constant with F(θ)of $CoZn_xTi_xFe_{2-2x}O_4$

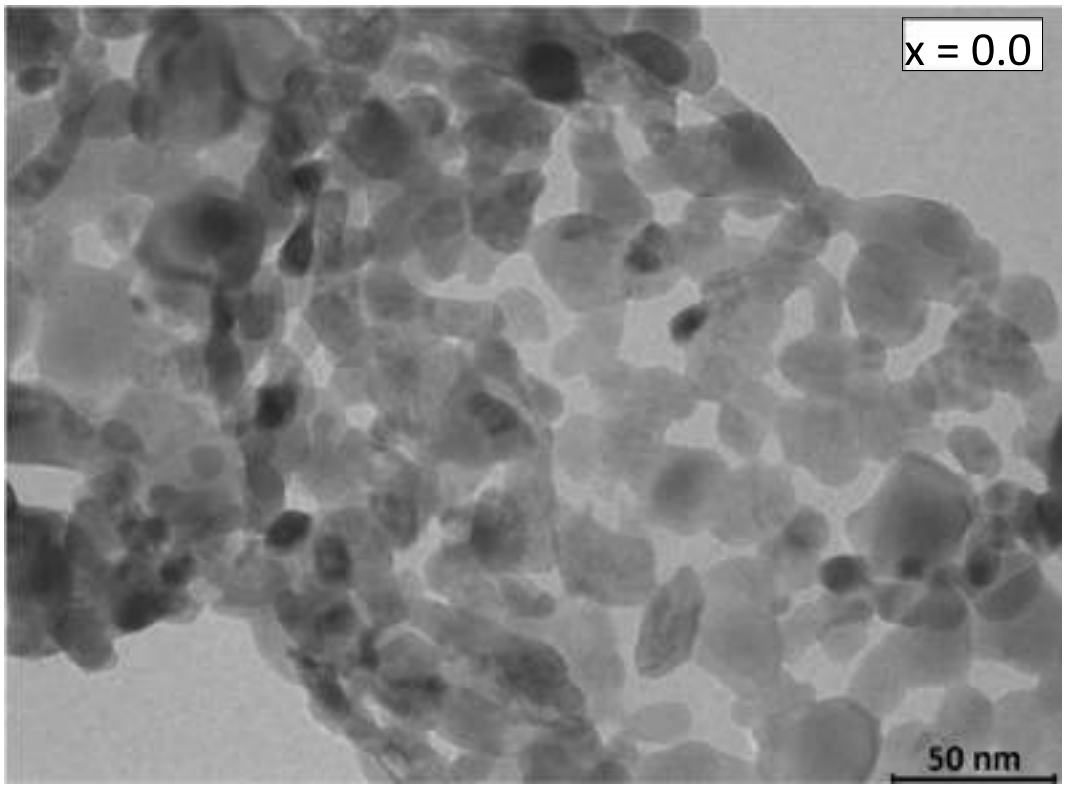

View Article Online
DOI: 10.1039/C5RA21522F

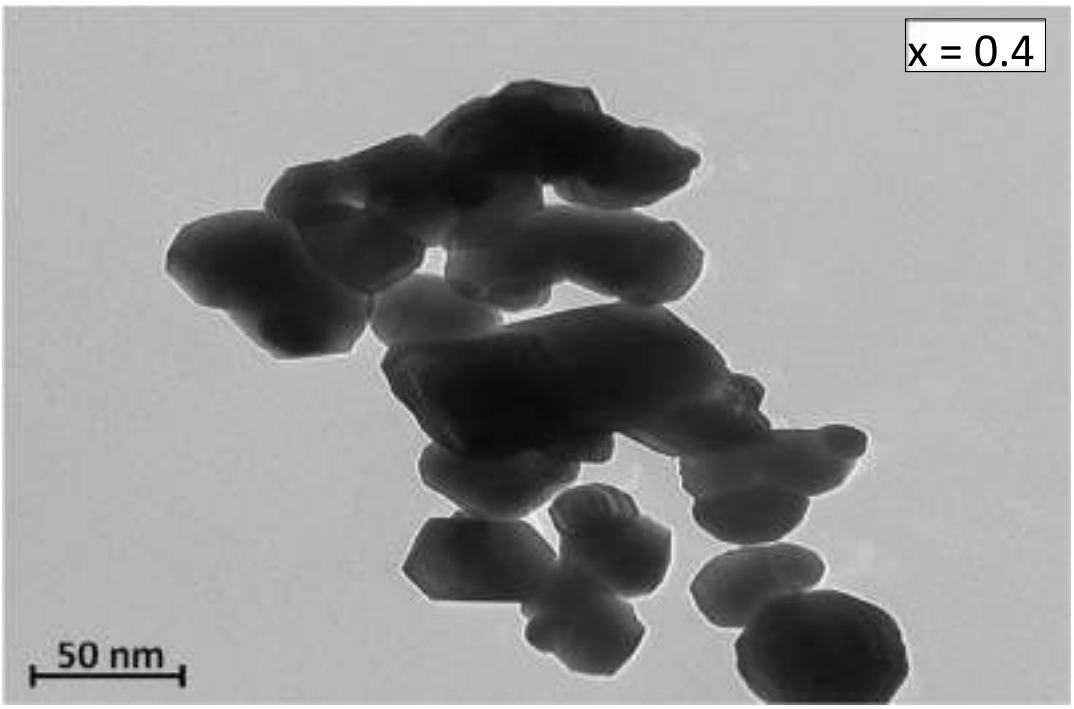

Fig. 5. TEM images of typical samples of $CoZn_xTi_xFe_{2-2x}O_4$

View Article Online
DOI: 10.1039/C5RA21522F

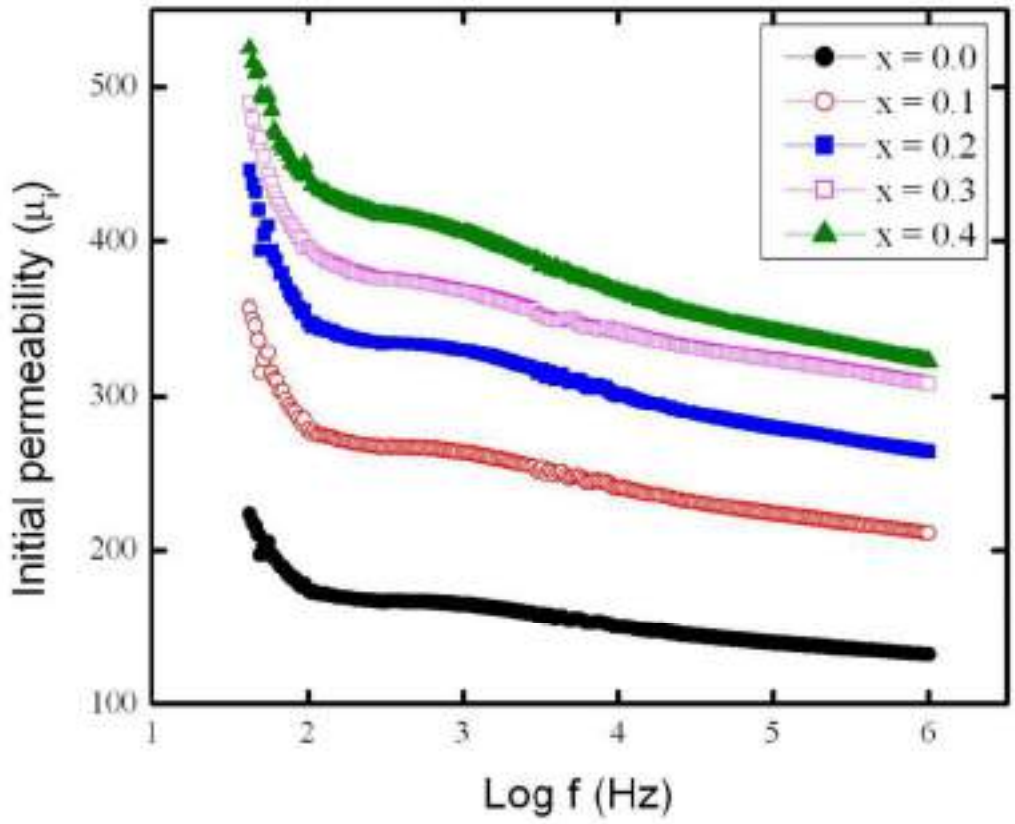

Fig. 6. Variation of initial permeability with logarithm of frequency

View Article Online
DOI: 10.1039/C5RA21522F

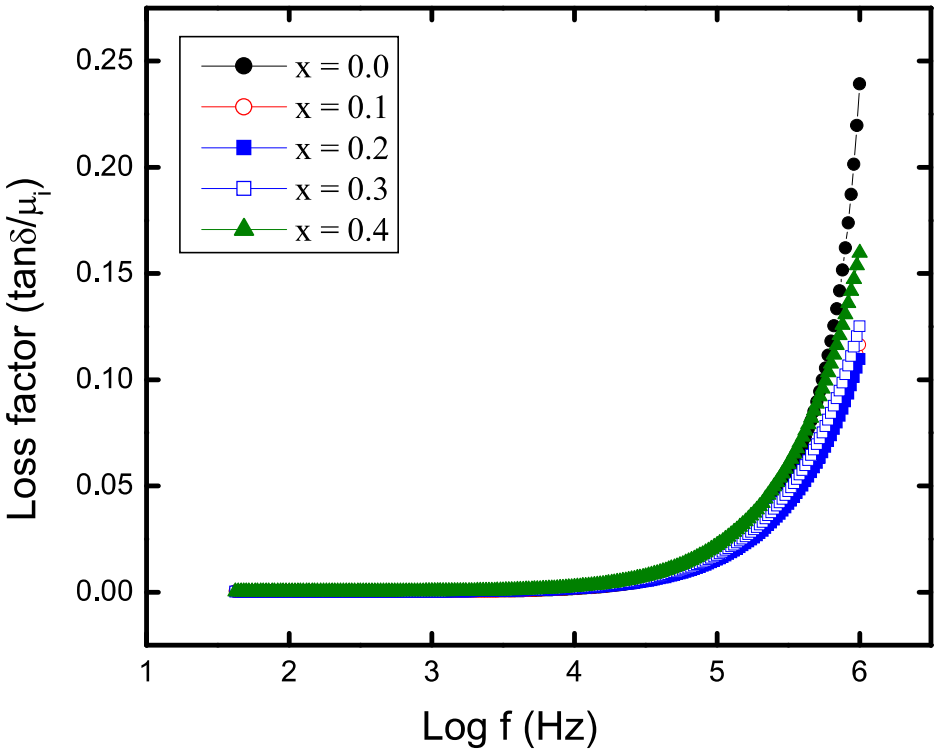

Fig. 7. Variation of loss factor with logarithm of frequency

View Article Online
DOI: 10.1039/C5RA21522F

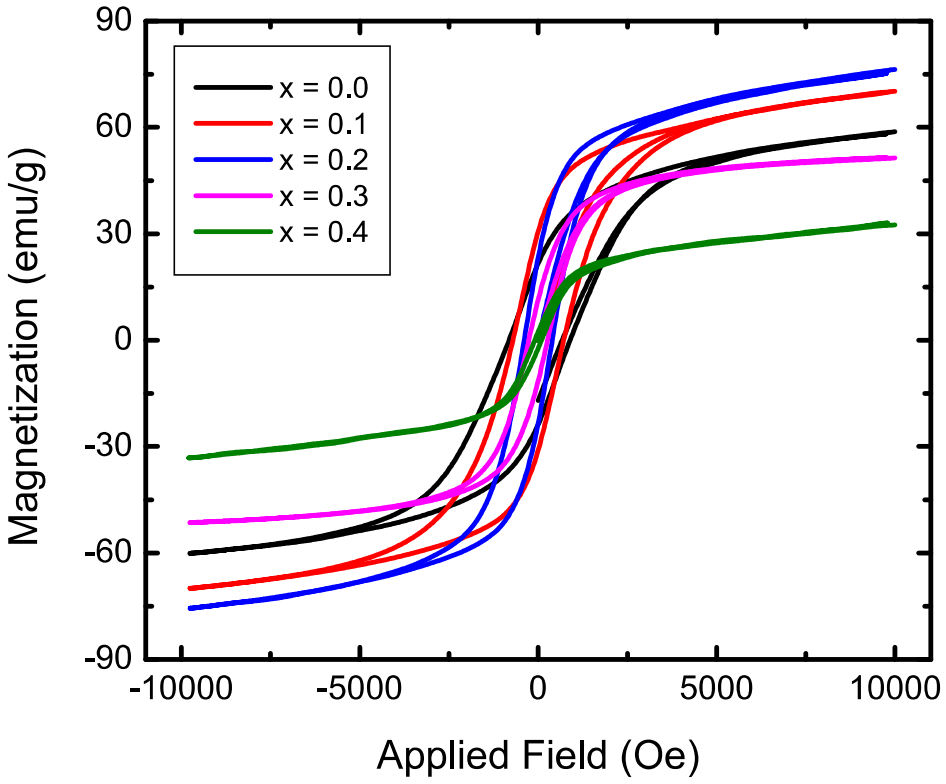

Fig. 8. Variation of magnetization with applied magnetic field

View Article Online
DOI: 10.1039/C5RA21522F

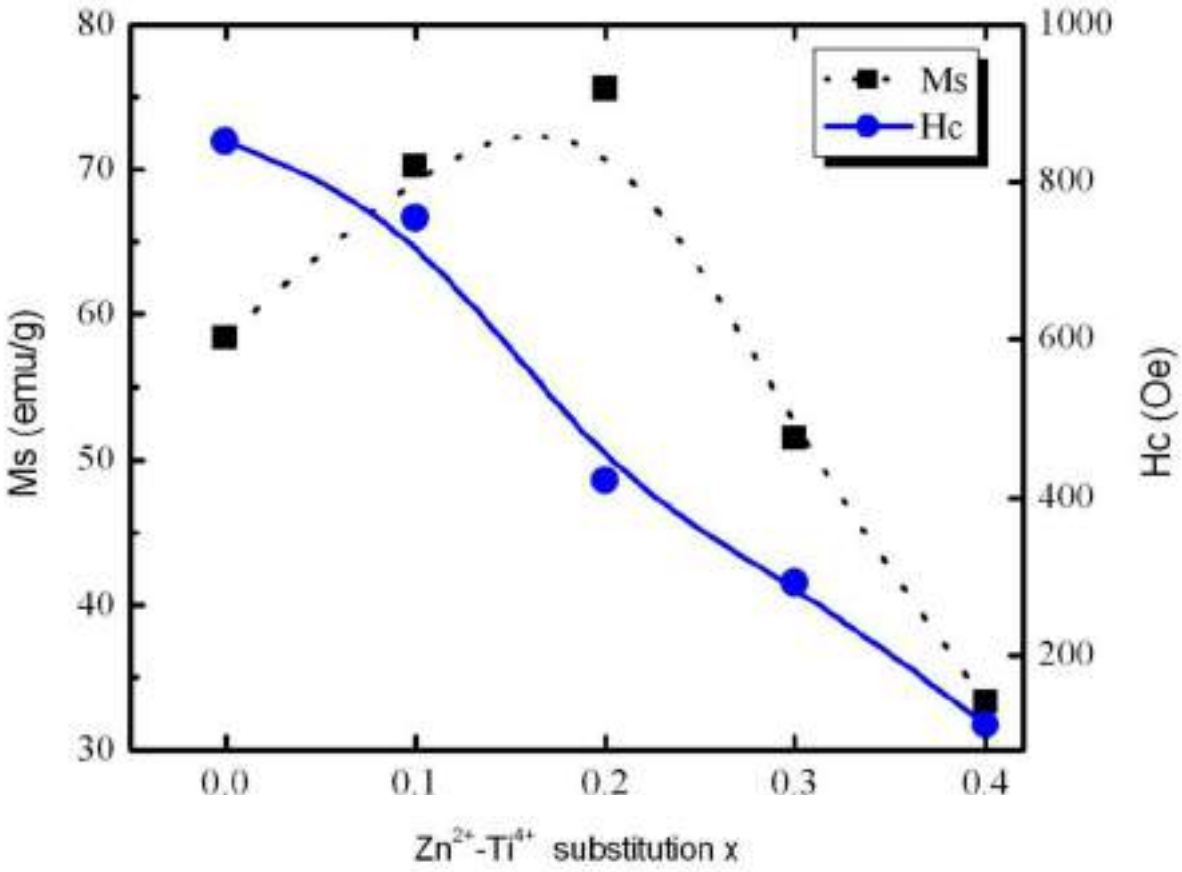

Fig. 9. Variation of saturation magnetization (Ms) and coercivity (Hc) with Zn^{2+}-Ti^{4+} substitution.

View Article Online
DOI: 10.1039/C5RA21522F

Fig. 10. Schematic representation of spin arrangements in $CoZn_xTi_xFe_{2-2x}O_4$ (a) for $x \leq 0.2$; (b) triangular (or Yafet–Kittel) for $x \geq 0.3$

View Article Online
DOI: 10.1039/C5RA21522F

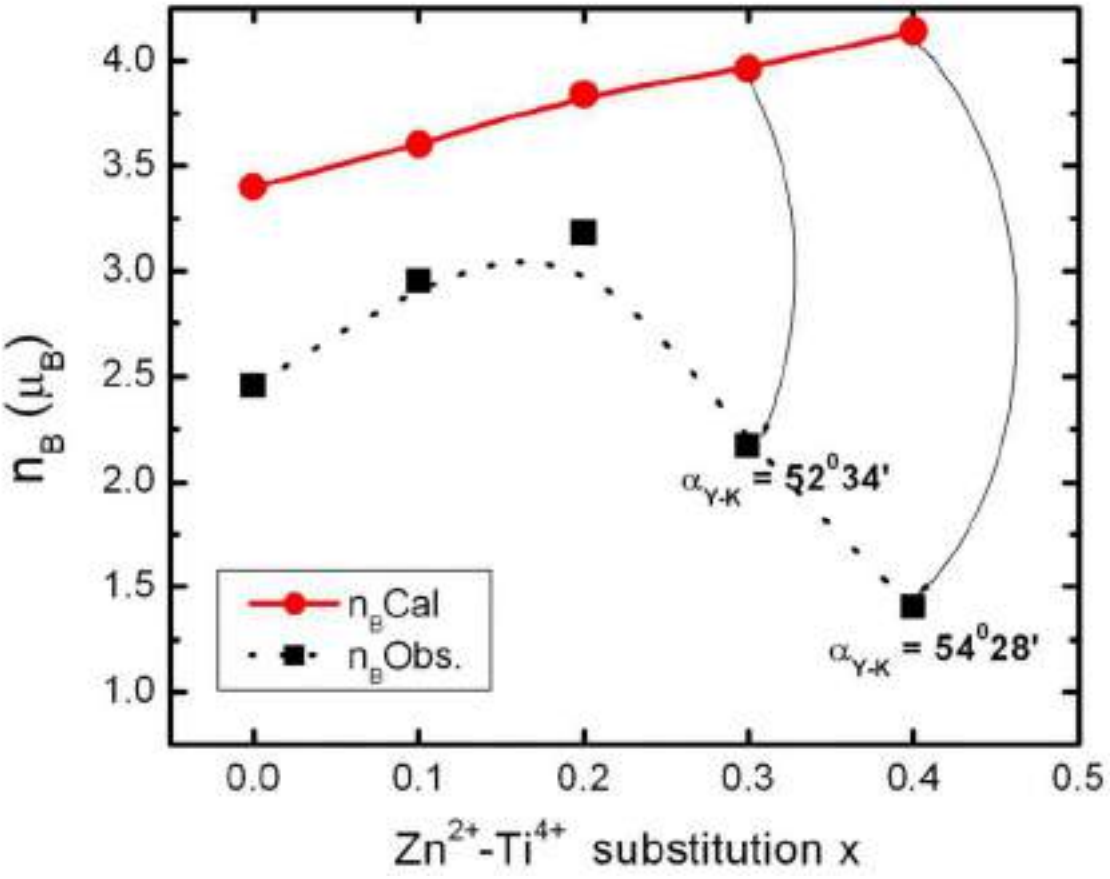

Fig. 11. Variation of observed (n_BObs.) and calculated (n_BCal.) magneton number with Zn^{2+}-Ti^{4+} substitution.

View Article Online
DOI: 10.1039/C5RA21522F

View Article Online
DOI: 10.1039/C5RA21522F

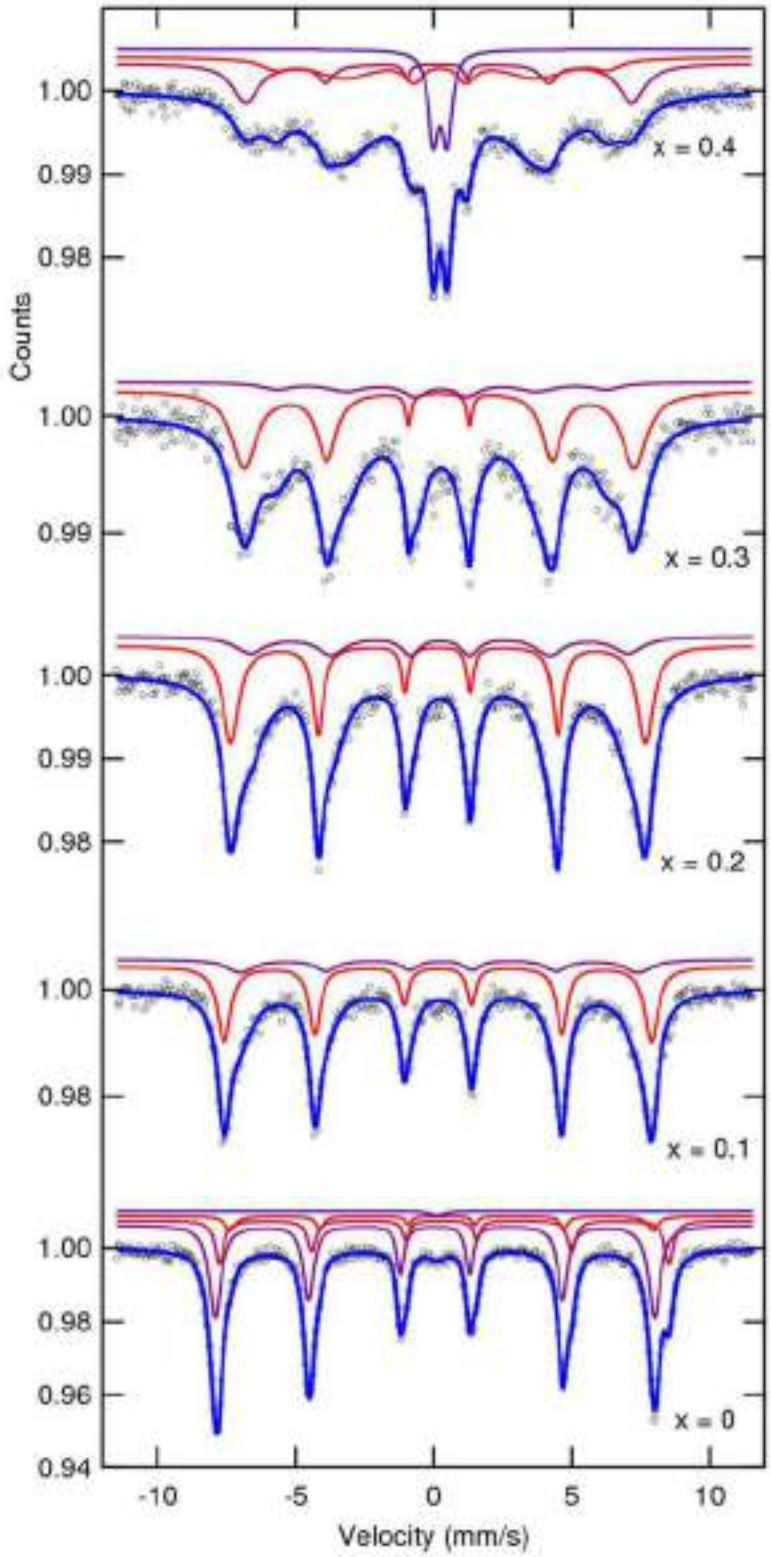

Fig. 12. Room temperature Mossbauer spectra of all the samples of $CoZn_xTi_xFe_{2-2x}O_4$